Auto-Resonant Detection Method for Optimized ZVS Operation in IPT Systems With Wide Variation of Magnetic Coupling and Load

FRANCESCA GRAZIAN [1] **(Student Member, IEEE), THIAGO BATISTA SOEIRO** [1] **(Senior Member, IEEE),**
PETER VAN DUIJSEN[2]**, AND PAVOL BAUER** [1] **(Senior Member, IEEE)**

[1] Electrical Sustainable Energy, Delft University of Technology, Delft 2628, The Netherlands
[2] Caspoc - Simulation Research, Alphen aan den Rijn 2401, The Netherlands

CORRESPONDING AUTHOR: FRANCESCA GRAZIAN (e-mail: F.Grazian@tudelft.nl).

This is a post-conference paper from the 29th IEEE International Symposium on Industrial Electronics (ISIE 2020).

ABSTRACT In wireless charging systems, the H-bridge converter's switching frequency is set close to the system's natural resonance for achieving optimized zero voltage switching (ZVS). Variations to the system's natural resonance are commonly tracked by following the changes in the resonant current's polarity, i.e., current zero-crossings. The main implementation challenge is accounting for the time delay between the real monitored current and the final resulting switches' commutations. This becomes critical at high switching frequencies, particularly when the magnetic coupling and loading vary widely. This paper proposes an auto-resonant detection method that continuously ensures optimized ZVS turn-on with the minimal circulating current over the operable range of magnetic coupling and load. The suggested implementation provides two split variable references for the resonant frequency detection, which adaptatively compensate for the propagation delay based on the resonant current slope. The auto-resonant scheme is benchmarked against the commonly employed method with fixed current detection references. The results highlight the auto-resonant strategy's advantages, namely extended operable range, wider ZVS turn-on region, ease start-up, and improved DC-to-DC efficiency. The auto-resonant features and functionality are verified experimentally with a 200 W low-voltage e-bike wireless charger. Finally, the benefits of the presented method are analytically explored for high-power applications by considering the H-bridge semiconductor losses of a state-of-art 50 kW wireless charging system.

INDEX TERMS Control, H-bridge converter, inductive power transfer, inverter, resonant converters, soft-switching, wireless charging, zero voltage switching.

I. INTRODUCTION

Wireless power transfer (WPT) systems have gained popularity in several battery charging applications such as implantable medical devices [1], consumer electronics [2], unmanned aerial vehicles [3], electric vehicles (EVs) [4]–[6], and maritime transportation [7], [8]. These applications generally work at different power levels, ranging from a few watts to hundreds of kilowatts. Nevertheless, most wireless charging systems work through non-radiative mid-range or near-field WPT that uses an electromagnetic field. This field's typical frequency can be in the order of kilohertz up to several megahertz [9]. According to [10], these applications are not suitable for the far-field microwave power transfer because of its directional nature and, more importantly, due to the more stringent human safety limits since the field's frequency is in the order of gigahertz. In high power applications, the magnetic field is commonly used to transfer energy between the power source and the receiving device [11], also named the primary and secondary circuits. This technology is called inductive power transfer (IPT) because the magnetic field exchange is realized through coupled coils. If passive components are used to compensate for the coils' reactive power, the IPT system becomes a resonant circuit that uses magnetic resonant coupling.
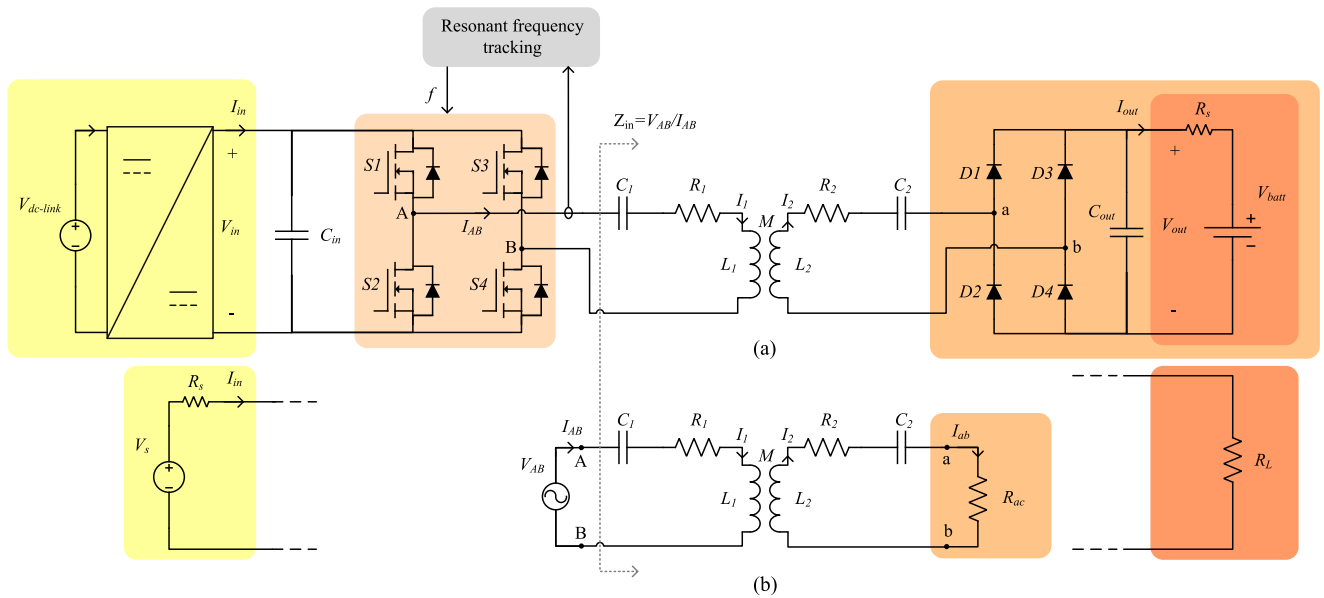
FIGURE 1. An IPT system with series-series (S-S) compensation: (a) Main circuit schematic; (b) Equivalent high-frequency circuit.

High power conversion efficiency is reached in a typical IPT system with magnetic resonant coupling by operating the circuit close to its natural resonant frequency such that the circulating reactive power is minimized. This can be achieved by controlling the operating frequency of the commonly employed H-bridge converter, of which a typical circuit schematic is shown in Fig. 1. A small amount of reactive current would flow in the circuit by setting the operating frequency slightly higher than the natural resonant frequency. This current should be high enough to guarantee the converter's switches to operate in soft-switching condition, i.e., zero voltage switching (ZVS) turn-on. This optimum frequency de-tuning would benefit not only the efficiency of the inverter but also the high-frequency electromagnetic compatibility (EMC) of the radiated magnetic field since the soft-switching operation reduces overshoots and ringing in the inverter's voltage and current waveforms. Consequently, to ensure high efficiency and adequate EMC, it is fundamental to accurately track the resonant frequency of the system.

In a practical implementation, the natural resonant frequency of an IPT system varies from the theoretical value due to the components' manufacturing tolerance, degradation, temperature rise, and more importantly, because of the change in the coils' equivalent self-inductance seen by the circuit which is mainly caused by different magnetic coupling conditions. Consequently, the frequency of the optimized ZVS point also varies and it must be tracked such that it is always matched by the inverter's operating frequency.

The most common methods to track the resonant frequency of IPT systems are summarized in Table I. The most commonly used tracking method is performed by tuning the active switching commands of the H-bridge converter with the changing of polarity of the resonant tank current as described in [23]–[31], i.e. by identifying the current's zero crossings. The main reasons are its implementation simplicity since it does not require communication between the primary and the secondary circuit and its fast reaction time. However, in a practical implementation, the necessary signal processing and measurement devices of the feedback controller introduces a time delay between the real monitored current and the final switches' commutation instants. It becomes critical to account for this delay when the circuit operates at high switching frequencies. Several researchers on traditional resonant converters have analyzed this issue [32]–[35], and their solutions employ dedicated circuits such as the phase-leading RL network [32]–[34] and the hysteresis-band compensation network [32]. Besides the traditional resonant converters, it is also interesting to evaluate how the propagation delay affects specifically IPT systems' performance, where, the magnetic coupling between the main coils and the loading conditions can vary in a wide operating range, which corresponds to the H-bridge converter's currents with different amplitude and resonant frequency. In IPT applications, the delay compensation has been acknowledged in [17], [19], [23]–[29]. In [23], [24], the control uses a field-programmable gate array (FPGA) to minimize this propagation delay. However, this solution would not be cost-effective, especially for low-power wireless charging systems. In [17], [19], this delay is compensated with an adjustable reference for the detection, which is not practical in a real application. On the other hand, [25]–[29] compensate for the propagation time delay by using a RC circuit as a phase-lead compensator. However, this solution follows a purely practical approach. Another conventional and simple way to compensate for this delay is performed by selecting two conservative (fixed) resonant current switching instants that guarantees ZVS turn-on for all active semiconductors,

TABLE I Summary of the Resonant Frequency Tracking Methods for IPT Systems. These Methods Have Two Possible Implementations. The First Option Uses Variable Passive Compensation and Fixed Operating Frequency. The Second Option Has Fixed Passive Circuits, and It Varies the Converter's Operating Frequency

Control concept	References	Properties			Implementation		
		Need of communication	Reaction time	Others	Variable compensation	Variable frequency	Searching algorithm
Detection of the minimum Z_r or Z_r	[12]–[14]	✗	>100 ms		[12], [13]	[14]	✓
Peak detection of the primary resonant current	[15], [16]	✗	>100 ms			[15], [16]	✓
PLL used for sensing the phase difference between: • V_{AB} and I_{AB} • V_{AB} and V_{C1} • V_{AB} and I_{ab} • I_{AB} and V_{ab}	 [17]–[19] [20] [21] [22]	 ✗ ✗ ✓ ✓	10-100 ms	[17]–[21] use comparators or zero-current detection • [17]: PLL as start-up circuit • [20]: higher bandwidth • [21] stands bifurcation • [22] stands bifurcation		[17]–[22]	✗
Zero-crossing detection of the converter's current	[23]–[31]	✗	Half of $\dfrac{1}{f_{sw}}$		[31]	[23]–[30]	✗

i.e. by forcing the circuit operation in the resonant tank's inductive region for all operating conditions. However, the forced operation too deeply in the inductive region may cause start-up problems in some operating points. Additionally, this strategy may cause low power conversion efficiency because an unnecessary large circulating reactive power will result at higher magnetic coupling and it will become critical at partial load conditions.

This paper proposes a time delay compensation method starting from an analytical and theoretical point of view. This results in a natural resonant frequency tracking method, named here as auto-resonant detection method, for the H-bridge converter used in IPT systems that is able to dynamically optimize the ZVS operation over different coils' coupling and loading conditions, i.e., it ensures a ZVS operation with minimal circulating reactive power. This method is self-calibrated by taking the information of the resonant tank current slope. Additionally, this paper highlights the advantages and impact of this delay's compensation in wireless charging systems which are particularly relevant for this application since the coils' coupling and the load can vary considerably.

The contributions of this paper are the following:
- A review on the resonant frequency tracking control methods used in IPT applications (see Table I).
- The analytical proof that the delay compensation is directly proportional to the inverter's current slope.
- The circuit implementation of the above-mentioned property as a feature of the auto-resonant control, validated both with simulations and experimentally.
- The benchmark of the auto-resonant control against the ZVS resonant converter's feedback control that uses constant detection levels when considering the application of e-bikes' wireless charging.
- The analytical proof that the proposed control can mitigate the semiconductor losses of the H-bridge converter's switches in a state-of-art 50 kW wireless charger.

It is important to point out that the proposed auto-resonant method defining the optimized ZVS switching instants can be adapted and utilized in most known feedback control schemes used in IPT systems. As described in [31], [36]–[38], non-isolated DC-DC converters or active H-bridge converters with appropriate feedback control loop for regulating the battery charging power could be implemented while the resonant converter's voltage gain could be tuned such that the efficiency of the resonant circuit is maximized. Therefore, the proposed auto-resonant method could be used for controlling the resonant converter voltage gain with the optimized ZVS while achieving the minimum circulating reactive current.

This paper is organized as follows. A design guideline for the converter controllability required by the auto-resonant detection method is proposed in Section II which is valid for the series-series (S-S) compensation network. Section III demonstrates analytically that the required delay compensation depends on the slope of the resonant tank current at the zero-crossing. The auto-resonant detection's implementation, the nominal operating waveforms, and the start-up strategy are also discussed. In Section IV, the circuit in Fig. 1 is simulated with the auto-resonant scheme while considering the application of e-bikes' wireless charging. Additionally, the proposed auto-resonant detection method is benchmarked against the traditional fixed reference scheme. In Section V, the auto-resonant detection functionality is demonstrated experimentally with a 200 W e-bike wireless charging prototype. The benefits for higher power applications are discussed in Section VI, when considering a state-of-art 50 kW wireless charger. Conclusions are summarized in Section VII.

II. DESIGN GUIDELINE - INVERTER CONTROLLABILITY

In H-bridge resonant converters, the ZVS turn-on of the MOSFETs can be achieved by operating in the equivalent inductive region of the resonant tank, i.e., when the converter's current lags the generated square wave voltage.

However, in inductive power transfer systems with magnetic resonant coupling, it might happen that the system has multiple resonant frequencies, which means that $\phi(Z_{in})$ is equal to zero for multiple frequencies and not only for the designed resonant frequency. This phenomenon takes the name of bifurcation or frequency splitting. It was first observed in [39], [40], then [21], [41]–[45] researched more on the topic. When bifurcation occurs, setting the H-bridge converter's operating frequency slightly higher than the natural resonance would place the operation in the equivalent capacitive region of the resonant tank that translates into a hard switching turn-on of the active switches.

To ensure that the ZVS turn-on of the H-bridge converter is achieved by operating at a frequency higher than the resonance, the S-S compensation network must operate for R_L values larger than $R_{L,bif}$ defined in (1).

$$R_{L,bif} = \frac{\pi^2}{8}\omega_0 L_2\sqrt{2(1-\sqrt{1-k^2})} \qquad (1)$$

If the condition $R_L > R_{L,bif}$ is always satisfied, the auto-resonant detection method will guarantee the ZVS turn-on for the whole output characteristic employed by the load.

III. AUTO-RESONANT DETECTION METHOD

A. MATHEMATICAL ANALYSIS

Taking as a reference Fig. 1(a), the ZVS turn-on of the active semiconductors can be achieved by switching the converter's legs before the zero-crossing of I_{AB}. In particular, [46]–[49] define in (2) the minimum amount of current I_{OFF} necessary to completely discharge the drain-source capacitance C_{ds} of the MOSFET in one bridge-leg, being the switched voltage $V_{ds,off} = V_{in}$, and t_{dead} the switching dead-time.

$$I_{OFF} > \frac{2 \cdot C_{ds}V_{in}}{t_{dead}} \qquad (2)$$

Similarly to [23]–[31], the turn-off current I_{OFF} can be tracked accurately by a zero-crossing detection circuit that senses the resonant tank's current i_{AB}, which detects when $i_{AB} = |I_{OFF}|$, and sends the control signals to the H-bridge converter's gate drivers. In particular, the detection of I_{OFF} can be realized by using two differential comparators of which one is used for the positive slope and the other for the negative slope of i_{AB}. By assuming that the measured current signal is $v_{i,A}$ and that $V_{I_{OFF}}$ corresponds to the measurement of I_{OFF}, theoretically the ZVS turn-on is achieved when the comparators' references V_{ref+}, V_{ref-} are equal to $|V_{I_{OFF}}|$. An example of these signals is shown in Fig. 2(a), where the operating frequency of i_{AB} is 85 kHz and $I_{OFF} = 2$ A. Thereby, the detection instant of I_{OFF} would vary if either the amplitude or the frequency of i_{AB} changes, which is shown by t_1, t_2 and t_3. The comparators are able to follow this change and to detect the same I_{OFF} by keeping V_{ref+} and V_{ref-} constant at $V_{I_{OFF}}$. By selecting I_{OFF} based on the worst operating condition that maximizes (2), V_{ref+} and V_{ref-} do not have to be adjusted in order to keep the optimized ZVS in different operating conditions. However, as discussed in Section I, a practical
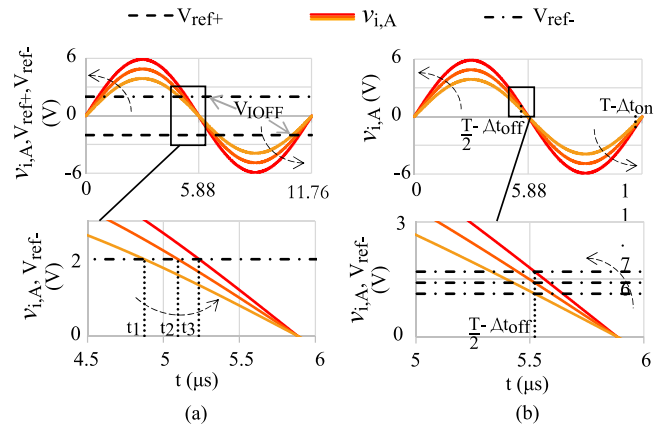

FIGURE 2. Voltage signal of the sensed resonant current $v_{i,A}$, and the references V_{ref+}, V_{ref-} that: (a) detect the current I_{OFF} which guarantees ZVS turn-on, (b) compensate for the control's delay Δt_{on}, Δt_{off}.

implementation needs to take into account the time delay between the detection times and the gating control signals to the active semiconductors introduced by the control circuit. It is interesting to investigate if the fixed references V_{ref+} and V_{ref-} in Fig. 2(a) can effectively compensate also for this propagation delay.

The total delay Δt is generally in the order of hundreds of nanoseconds (ns), which might not be negligible in high-frequency applications where the resonance period becomes comparable to the delay times. As a first approximation, Δt is considered to be constant, which is reasonable for a certain temperature and supply voltage of the typically used analog electronics. Additionally, it is assumed that the delay time in the detection of the positive slope of i_{AB} is Δt_{on}, while for the negative slope is Δt_{off}. This means that V_{ref+} must compensate for the delay Δt_{on}, and V_{ref-} must compensate for the delay Δt_{off}. Considering the zero-crossing of the two slopes separately has the potential to account for possible asymmetries in the current waveform and the differences that might exist in the on-/off-reaction times of the components. Even though Δt_{on} and Δt_{off} are constant, Fig. 2(b) shows that the value of V_{ref+} and V_{ref-} should vary to compensate for the same delay if the amplitude of i_{AB} changes. A similar variation in V_{ref+} and V_{ref-} would be also necessary if the frequency of i_{AB} varies. This implies that the fixed voltage references used in Fig. 2(a) do not effectively detect I_{OFF} in a real circuit where the propagation delay is present.

In [50], it has been demonstrated mathematically that the reference voltage level that compensates for the delay time depends on the slope of the current i_{AB} in the proximity of the zero-crossing. This is valid if the converter's current i_{AB} approximates a sinusoid which can be expressed as

$$i_{AB} = i_{AB}(t) = \sqrt{2}I_{AB}\sin(2\pi f t) = \sqrt{2}I_{AB}\sin(\omega t) \qquad (3)$$

This analysis relies on the small angle approximation for which a sinusoidal waveform can be approximated as a linear

curve in the proximity of its zero-crossing:

$$\sin(\omega t) \approx \omega t$$
$$\Updownarrow \qquad\qquad (4)$$
$$-\frac{\pi}{6} < (\omega t + a\frac{T}{2}) < \frac{\pi}{6} \quad (\forall a \in \mathbb{Z})$$

By using these assumptions, the measured current signal $v_{i,A}$ can be approximated as in (5).

$$v_{i,A}(t) = \sqrt{2}V_{i,A}\sin(\omega t) \approx \sqrt{2}V_{i,A}\omega t \qquad (5)$$

As a result, the reference voltages V_{ref+} and V_{ref-} that respectively compensate for the delays Δt_{on} and Δt_{off} are shown in (6) and (7), where $\frac{d}{dt}v_{i,A}$ is the time derivative of the measured current signal in the vicinity of the $v_{i,A}$ zero-crossing. This means that the reference voltage that compensates the time delay depends on the slope of the current at the zero-crossing.

$$V_{ref+} \approx \sqrt{2}V_{i,A}\omega\Delta t_{on} = \frac{d}{dt}v_{i,A}(t)\Delta t_{on} = V_{diff+} \qquad (6)$$

$$V_{ref-} \approx \sqrt{2}V_{i,A}\omega\Delta t_{off} = \frac{d}{dt}v_{i,A}(t)\Delta t_{off} = V_{diff-} \qquad (7)$$

From this analysis, the concept of the auto-resonant detection method has been created, which is appropriate for IPT applications where the operating conditions are not constant. For instance, the amplitude and frequency of the H-bridge's current i_{AB} vary due to changes in the coil's mangetic coupling or in the loading condition. The auto-resonant scheme adapts the references for the detection of i_{AB} based on the slope of the current at the zero-crossing to compensate continuously for the control's propagation delay such that the optimized ZVS point is tracked accurately.

This concept is based on the assumption that the converter's current has a sinusoidal shape such that the first harmonic approximation is valid. This assumption is reasonable for IPT systems that employ a S-S compensation because the converter's current also flows through the primary resonant circuit that acts as a low-pass filter. Moreover, the same current flows through the primary coil which cannot be highly distorted because, in that case, the radiate electromagnetic field could cause serious EMC issues. On the other hand, when the double-sided LCC is used as a compensation [47], the resonant tank's current might be distorted due to the presence of multiple resonant frequencies of the passive circuit. In that case, the measured current signal could be filtered out (e.g. with a low-pass filter) such that only its fundamental component is used in the auto-resonant scheme. After that, the relationship between the optimized ZVS point and the current's fundamental component could be found depending on the distortion level of the current.

Summarizing, it has been found that the optimized ZVS point can be continuously tracked by the detection reference V_{ref} which is composed of two terms, as shown in (8). The first term V_{IOFF} is fixed and contributes to the detection of the turn-off current I_{OFF} in (2) which is shown in Fig. 2(a). On the other hand, the second term V_{diff} is variable and it dynamically compensates for the delay introduced by the control circuit. This variable reference has been shown in Fig. 2(b)
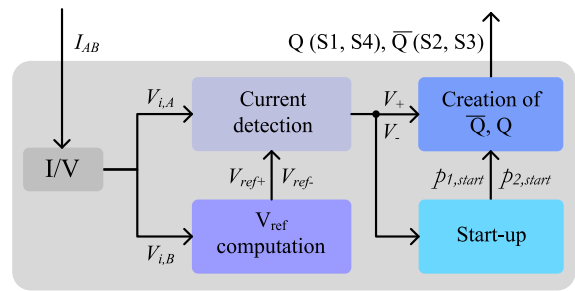

FIGURE 3. Block diagram of the auto-resonant detection method.

and, according to (6) and (7), its value depends on the slope of i_{AB} at the zero-crossing and on the delay time Δt introduced by the control.

$$V_{ref} = \underbrace{V_{IOFF}}_{fixed} + \underbrace{V_{diff}}_{variable} \qquad (8)$$

The generic references V_{ref}, V_{diff} and delay time Δt are used when it is not required in the discussion to distinguish between the positive and the negative slope of i_{AB}.

B. IMPLEMENTATION: NOMINAL OPERATION AND START-UP

The auto-resonant scheme generates the control signals for the MOSFETs of the H-bridge converter in Fig. 1(a). The current i_{AB} is taken as the input signal, while the output signals that control the converter are Q and $\overline{Q}$. The signal Q controls the switches S1 and S4, while $\overline{Q}$ controls the switches S2 and S3. The block diagram of the proposed control is shown in Fig. 3, and the circuits used in each block are shown in Fig. 4. The converter current i_{AB} is measured, and the correspondent signal $V_{i,B}$ is used to create the references V_{ref+} and V_{ref-}. According to (8), both voltage references are composed of the fixed term V_{IOFF} and the variable term V_{diff}. The fixed term V_{IOFF} is given by the optimized ZVS point of the MOSFET which can be calculated through (2). The variable term V_{diff} depends on the derivative of i_{AB} at the zero-crossing, and it can be calculated according to (6) and (7). To realize the variable voltage V_{diff}, the implementation uses a differentiator circuit, which output is

$$V_{o,B} = -C_{diff}R_{diff}\frac{dV_{i,B}}{dt} \qquad (9)$$

The derivative $V_{o,B}$ is then rectified and filtered. The last filtering stage composed of R_2, C_2 and R_4, C_4 smooths out the ripple of the rectified voltage signals. However, the dynamic behavior of V_{diff} is important because it needs to reflect the instantaneous variations in the slope of i_{AB} that might occur during transients. This means that the time constant of the filter must have the same order of magnitude as the switching period. The two terms V_{IOFF} and V_{diff} are then summed to achieve the reference voltage V_{ref} in (8). Once the parameters are tuned, the detection must be evaluated at $k = k_{max}$ to verify if the inverter switches at the optimized ZVS
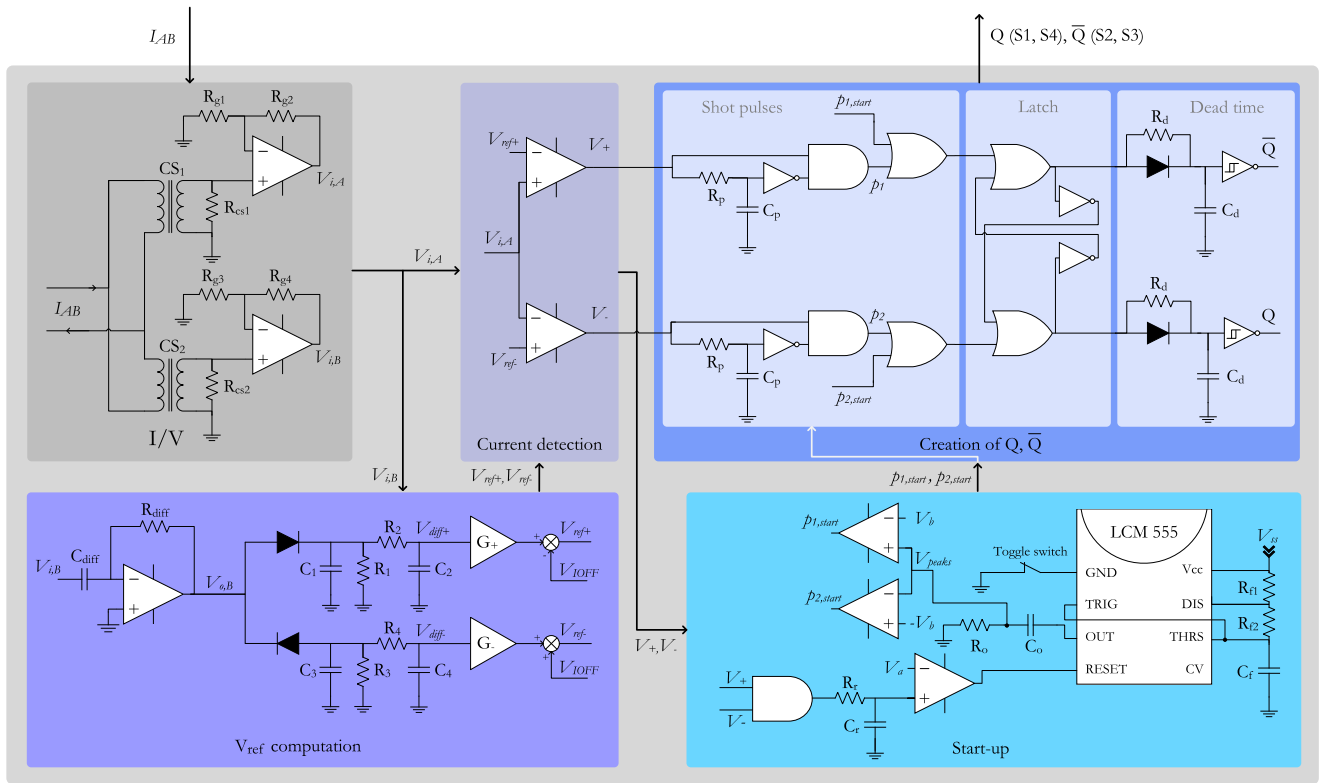
FIGURE 4. Implementation of the auto-resonant detection method based on the block diagram of Fig. 3.

point for the implemented V_{ref}. If that is not the case, the passive components must be re-tuned until the desired I_{OFF} is reached. It is preferable to start the parameters tuning from the maximum coupling condition because, thereby, the S-S compensation network requires a converter's resonant current with relatively low amplitude that might complicate the reaching of the steady-state operation. After that, the control can be validated and fine-tuned for the minimum-allowed alignment condition ($k = k_{min}$).

The resulting references V_{ref+} and V_{ref-} are compared to the other measured signal $V_{i,A}$ to detect $|I_{OFF}|$. As a result, the outputs are the two square waves V_+ and V_- produced by the analog comparators, which are qualitatively shown in Fig. 5(a). The signals V_+ and V_- might overlap because they are completely independent of each other. Considering that V_+ is the control signal related to the positive slope zero-crossing of i_{AB}, while V_- is related to the negative slope zero-crossing of i_{AB}, the part of interest of V_+ and V_- is just the one related to their rising edge. Therefore, to guarantee that there is no overlap, V_+ and V_- are shortened into the pulses p_1 and p_2, which only focus on their parts of interest. The qualitative representation of p_1 and p_2 is shown in Fig. 5(b). After this, the intervals of time in which p_1 and p_2 assume the high value are again extended, such that each signal becomes low as soon as the other one becomes high. This is implemented through a latch circuit. Finally, the last step consists in setting up the optimal t_{dead} because, as explained in [49], it is important that

t_{dead} is long enough to ensure the actual ZVS turn-on but, at the same time, t_{dead} must be over before i_{AB} changes polarity such that the current flow would naturally switch from the anti-parallel diode to the MOSFET. At this point, the gating signals Q and $\overline{Q}$ are created, and they are sent to the gate drivers. Their qualitative representation is shown in Fig. 5(c).

This concept of auto-resonant detection method can be implemented using analog components. The analog implementation complicates the start-up of the power transfer because, when i_{AB} is zero, the comparators will not work. Therefore, to start the power transfer, the circuit needs to excite the flow of I_{AB}. A start-up circuit is used to create the starting short pulses $p_{1,start}$ and $p_{2,start}$, which initially substitute the nominal p_1 and p_2. These starting pulses are generated by the timed oscillator LCM555 such that their frequency is slightly higher than the nominal. This ensures that the operation is in the inductive region of the resonant tank. As soon as the detection circuit creates the output signals V_+ and V_-, the start-up is disabled, $p_{1,start}$ and $p_{2,start}$ are stopped, and the nominal operation takes place.

IV. CIRCUIT SIMULATIONS

As a first proof of concept, the proposed start-up strategy and the auto-resonant scheme in Fig. 4 has been validated through simulations of the circuit in Fig. 1 adapted to the prototype of a 200 W e-bike charger which will be discussed in Section V. The simulations have been executed in LT Spice
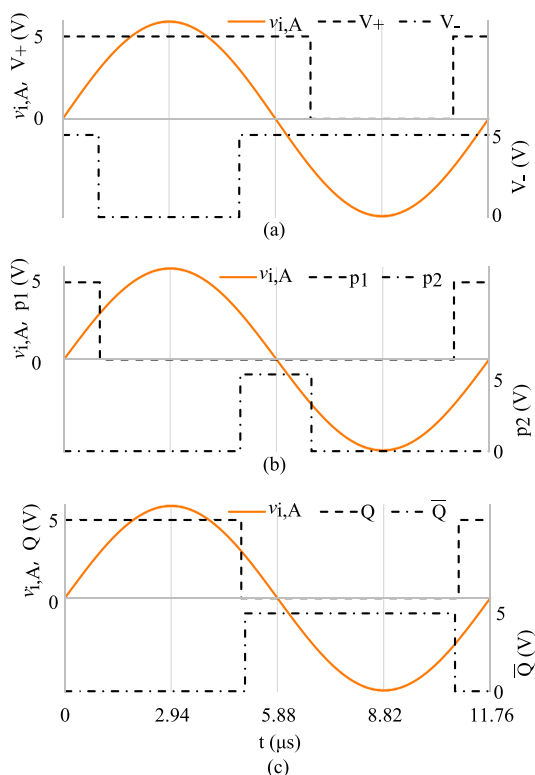
FIGURE 5. Qualitative waveforms of the auto-resonant detection scheme that refer to the block diagram in Fig. 1(c). (a) Comparators' output voltages V_+, V_-. (b) Short pulses p_1, p_2. (c) Output signals Q, $\overline{Q}$ to control the gate driver.

TABLE II Parameters of the 200 W E-Bike Laboratory Set-Up Which Have Been Used for Both Simulated and Experimental Results

k	$L_1(\mu H)$	$L_2(\mu H)$	$C_1(nF)$	$C_2(nF)$	$I_{OFF}(A)$
0.266	56.85	45.51			
0.201	52.36	42.62	67.7	77.7	2
0.147	50.76	40.97			

$R_{1,2}(\Omega)$	$R_s(\Omega)$	$V_{batt}(V)$	$P_{out}(W)$	$C_{in,out}(\mu F)$
0.13	0.5	40	200	60

with a maximum time step of 10 ns. An inductance of 1 nH is placed between the drain pins of the high-side MOSFETs and the source pins of the low-side MOSFETs for representing an equivalent parasitic inductance due to the wiring of the printed circuit board (PCB) and the components' package leads. The circuit parameters used are shown in Table II which describe the laboratory prototype discussed in Section V. From Table II, it is possible to notice that the equivalent values of the self-inductances L_1 and L_2 of the practical IPT system are dependent on the magnetic coupling k. This means that, for the same compensation capacitance, the natural resonant frequency of the system would vary. For instance, the resonant frequency of the primary resonant circuit would vary from 81.1 kHz to 85.9 kHz when the magnetic coupling changes from k=0.266 to k=0.147. Since the operating frequency of the inverter is going to be slightly higher than the resonant frequency, the values of C_1, C_2 and V_{batt} have been chosen
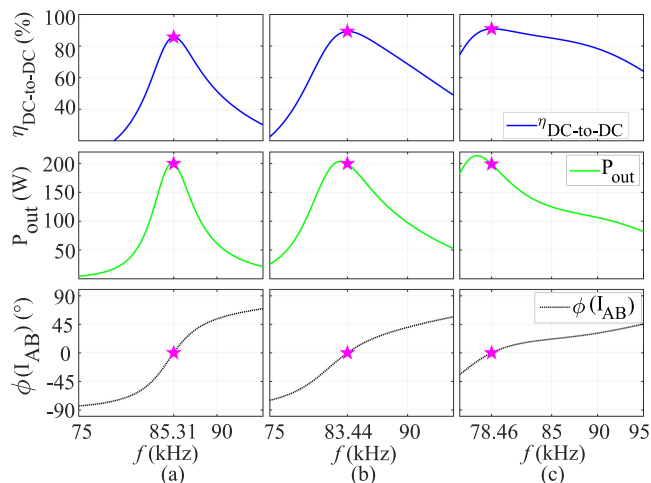

FIGURE 6. Frequency-domain analysis of the efficiency $\eta_{DC-to-DC}$, output power P_{out}, and phase $\Phi(I_{AB})$ at: (a) k=0.147, (b) k=0.201, (c) k=0.266.

TABLE III Example of Delays Introduced by ICs and the Gate Driver

Component			Delay (ns)[1]	
Type	Name	n.	Δt_{on}	Δt_{off}
Opamp (3 MHz)	TL071	1	100	100
Diff. comparator	LM211	1	115	165
Schmitt-Trigger Inv.	SN74LVC1G14	1	6	6
INVERTER gate	SN7404	2	15	15
AND gate	SN7423	1	27	19
OR gate	SN7408	2	15	22
Gate driver	IR 2110	1	150	120
[1] Datasheet @25 °C		Total	458	462

such that the frequency that maximizes the DC-to-DC efficiency of the IPT system is slightly higher than the resonant frequency for the entire k range as shown in Fig. 6, for the target $P_{out} = 200$ W.

To match the target output power of 200 W at different magnetic coupling, the input voltage of the converter V_{in} can be controlled through a DC/DC converter as shown in Fig. 1. The input voltage source $V_{dc-link}$ with the DC/DC converter has been modeled as a controllable DC power supply V_s with the series resistance R_s. On the other hand, the constant-voltage behavior of the battery has been modeled as a DC power supply set at 40 V with the series resistance R_s.

The total delay introduced by the control circuit is estimated in Table III based on the circuit implementation in Fig. 4. There is a small unbalance between the on- and off- reaction time of the components, and this can be accounted for by treating separately the detection of the positive and negative slope, as discussed in Section III. In the simulations, Δt_{off} and Δt_{off} of Table III have been imposed to the gating control signals Q and $\overline{Q}$ as shown in Fig. 2(b). Additionally, by solving (2) for the worst case scenario, the ZVS turn-on can be achieved for $I_{OFF} = 2$ A with $t_{dead} = 150$ ns.

Fig. 7 shows the simulated waveform at $k = 0.266$, which have been achieved by imposing $V_s = 42.8$ V. At
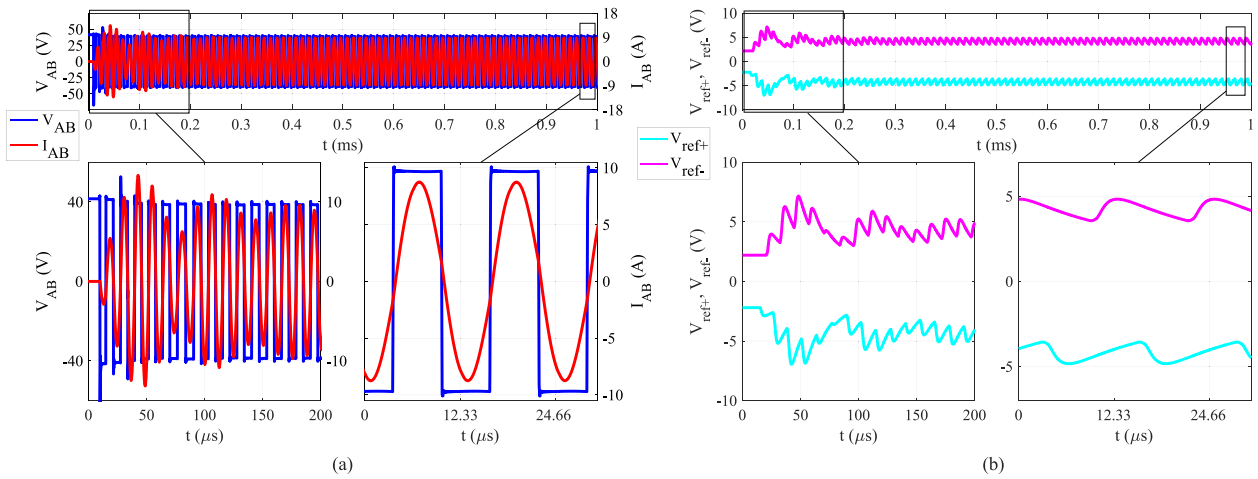
FIGURE 7. Circuit simulations that use the auto-resonant detection method at k=0.266 and $P_{out} = 200$ W ($V_s = 41.6$ V, $f_{sw} = 81.1$ kHz). Circuit waveforms measured: (a) Converter's output voltage V_{AB} and current I_{AB}, (b) Detection voltage references V_{ref+} and V_{ref-}.
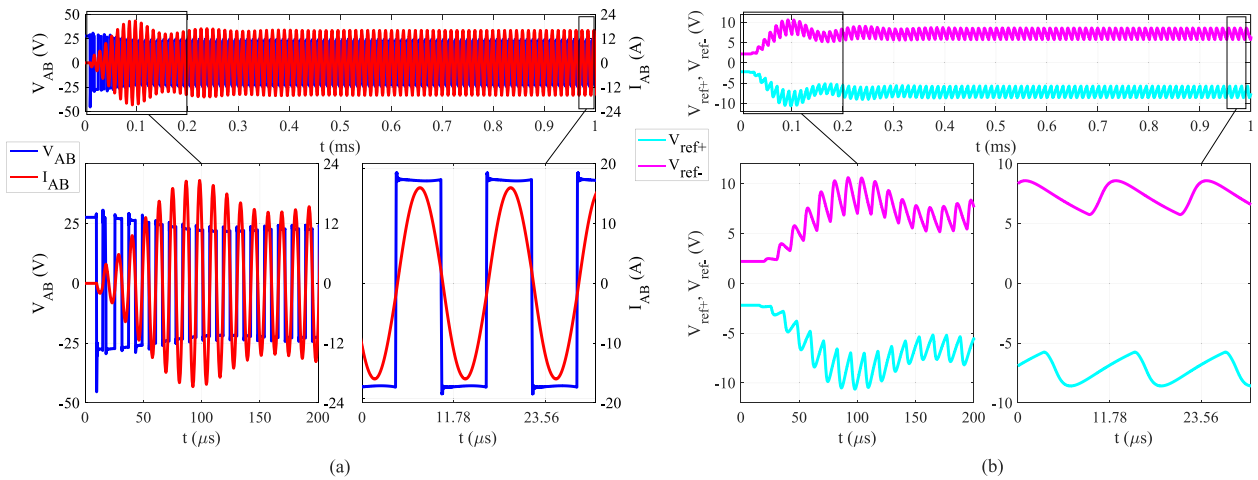

FIGURE 8. Circuit simulations that use the auto-resonant detection method at k=0.147 and $P_{out} = 200$ W ($V_s = 27.6$ V, $f_{sw} = 84.9$ kHz). Circuit waveforms measured: (a) Converter's output voltage V_{AB} and current I_{AB}, (b) Detection voltage references V_{ref+} and V_{ref-}.
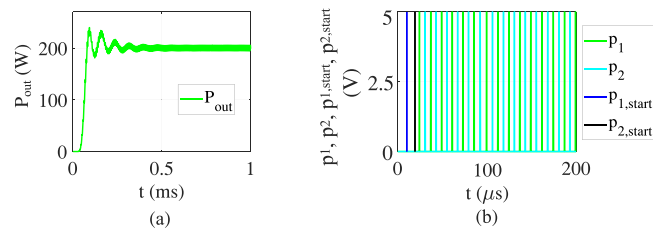

FIGURE 9. Circuit simulations that use the auto-resonant detection method at k=0.266: (a) output power P_{out} from the start-up to the steady-state operation, (b) starting pulses $p_{1,start}$, $p_{2,start}$ and nominal pulses p_1, p_2.
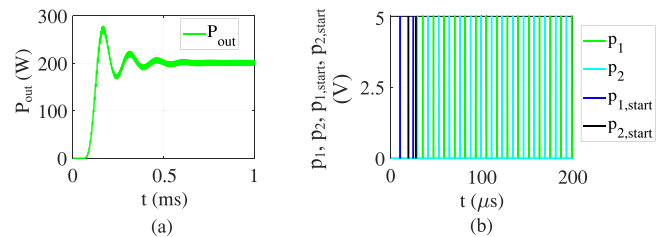

FIGURE 10. Circuit simulations that use the auto-resonant detection method at k=0.147: (a) output power P_{out} from the start-up to the steady-state operation, (b) starting pulses $p_{1,start}$, $p_{2,start}$ and nominal pulses p_1, p_2.

the steady-state operation, it is possible to detect I_{OFF} with V_{ref-}, $V_{ref+} = \pm3.6$ V. On the other hand, Fig. 8 shows the simulated waveform at k=0.147, which have been achieved by imposing $V_s = 27.8$ V. While for this magnetic coupling condition, it is possible to detect the same I_{OFF} with

V_{ref-}, $V_{ref+} = \pm6.4$ V at the steady-state operation. Thanks to the dynamic change of V_{ref+} and V_{ref-}, the ZVS turn-on is achieved for the steady-state operation and for the majority of the start-up transient. The hard switching operation during a few switching cycles does not affect the low voltage silicon
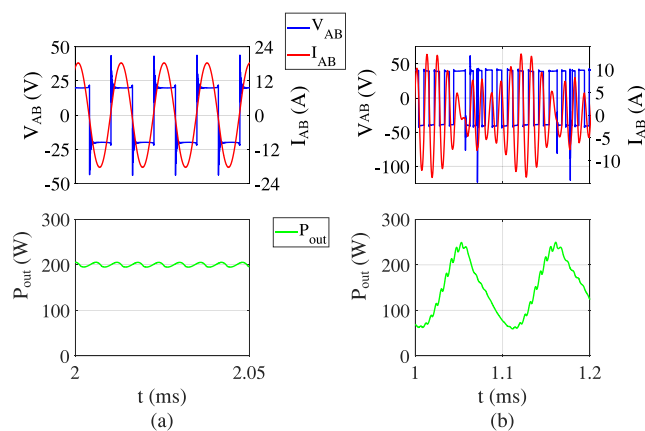
FIGURE 11. Circuit simulations that use the resonant frequency tracking with fixed reference for the zero-crossing detection. Circuit waveforms: (a) at $k=0.147$ with V_{ref+}, V_{ref-} tuned at $k=0.266$, (b) at $k=0.266$ with V_{ref+}, V_{ref-} tuned at $k=0.147$.

MOSFETs, particularly because of their low switching-energy loss. Then, V_{ref+} and V_{ref-} stabilize to the final value that has been set automatically by the auto-resonant detection method depending on the derivative of the primary current at the zero-crossing.

According to Fig. 9(a) and Fig. 10(a), it possible to notice that the target output power of 200 W is reached at the steady state operation for both values of k. This is achieved by regulating V_s. Furthermore, Fig. 9(b) and Fig. 10(b) show that the nominal operation of the auto-resonant control begins after the starting pulses $p_{1,start}$ and $p_{2,start}$ are sent for a few switching cycles. Once the amplitude I_{AB} is high enough, $p_{1,start}$ and $p_{2,start}$ are automatically disabled and the nominal pulses p_1 and p_2 take over.

A. COMPARISON WITH THE FEEDBACK CONTROL THAT USES FIXED REFERENCES

In IPT applications, the detection scheme with fixed or empirically adjustable references is commonly employed due to its implementation simplicity. These fixed detection references to the comparators are tuned at either the maximum or minimum coupling condition. It is fundamental to benchmark the proposed detection method with the traditional scheme that uses fixed references to verify the advantages. The comparison has been executed by using the circuit parameters in Table II, taking as a reference the circuit in Fig. 1(a).

First, the detection circuit with fixed voltage references has been tuned to achieve the ZVS turn-on at the steady-state operation for $k=0.266$, i.e., to the fixed references $V_{ref-}, V_{ref+} = \pm 3.6$ V. As a consequence, at that coupling condition, the circuit waveforms are equivalent to the ones achieved by using the auto-resonant control. It is more interesting to evaluate the operation at $k=0.147$, which is shown in Fig. 11(a). The semiconductor switches would operate in hard-switching condition because V_{ref+}, V_{ref-} are lower than the ones needed for the ZVS turn-on in Fig. 8(b).

After that, the detection circuit with fixed voltage references has been executed by tuning the reference voltages to achieve the ZVS turn-on at the steady-state operation for $k=0.147$, i.e., to the fixed references $V_{ref-}, V_{ref+} = \pm 6.4$ V. This means that, at that coupling condition, the circuit waveforms are equivalent to the ones achieved by using the auto-resonant scheme. However, Fig. 11(b) shows that the operation at $k=0.266$ does not reach the steady-state. This occurs because the higher voltage references set the operation further in the inductive region, which lowers the converter current's amplitude during the start-up transient. Thus, the current can become comparable or even lower than the detection value. This can be critical in low power applications where the amplitude of the current is in the same order of magnitude as the converter's current. Thereby, the variable detection references implemented in the auto-resonant method are essential for enabling the start-up of the power transfer. Besides, in high power applications, this behavior leads to unnecessary circulating reactive power and higher switch-off current that lower the power transfer efficiency. This is preliminary investigated in Section VI.

V. EXPERIMENTAL VERIFICATION

After the circuit simulations, it is important to prove the functionality of the auto-resonant control experimentally. The 200 W e-bike wireless charging laboratory prototype in Fig. 12 has been used. The implemented analog auto-resonant detection method is particularly interesting for the charging of e-bike since it is cost-effective and, as explained in Section IV-A, it enables the start-up at this relatively low-power. When considering an e-bike's battery with a nominal voltage of 40 V and the typical amperage of 10 Ah, a 200 W charger can complete onefull charging cycle in two hours.

The circuit schematic is shown in Fig. 1(a), and the main circuit parameters are summarized in Table II. The primary and secondary coils are made of a U-shape ferrite core, and the latter is confined in a sturdy plastic case for mechanic stability. The primary coil is embedded in a charging tile, while the secondary coil consists of the double-kick stand of the bike, as illustrated in Fig. 13(a). The prototype of the coils is shown in Fig. 13(b), and Fig. 13(c)-(e) represent the coils' alignment from the maximum to the minimum coupling condition correspondent to $k=0.266$, $k=0.20$, and $k=0.147$, respectively. Since the coils have a similar structure that resembles a U-shape magnetic core, they have a similar magnetic field distribution. Consequently, L_1 and L_2 have a similar variation trend as shown in Table II when the relative position between the coils changes. In this configuration, it is possible to ensure that the primary and the secondary circuits have similar resonant frequency even at different magnetic coupling conditions. In this application, it is important to ensure that the e-bike charging system is operable in a wide range of coils' alignments since the cyclist has some freedom in parking the e-bike. More details on this e-bike charging station can be found in [51].
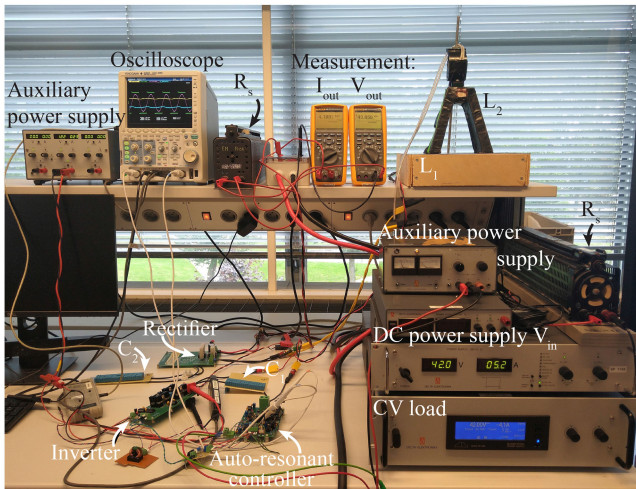
FIGURE 12. Laboratory prototype of a 200 W e-bike wireless charging system used to test the proposed auto-resonant detection method.
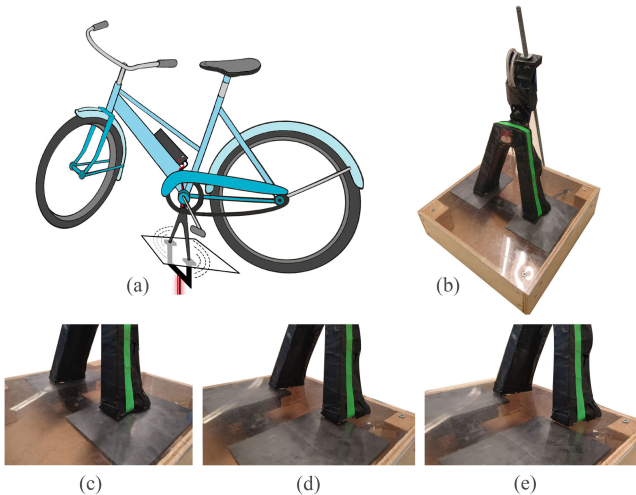

FIGURE 13. Laboratory prototype the main coils used for a 200 W e-bike wireless charging system. (a). Animation of the e-bike. (b) Overview of the aligned coils. Coils' alignment for: (c) k=0.266, (d) k=0.201, (e) k=0.147.

The measured circuit waveforms at k=0.266 are shown in Fig. 14 and Fig. 15, while the measurements at k=0.147 are shown in Fig. 16. Additionally, the proposed auto-resonant scheme benchmark against the feedback control with fixed references is shown in Fig. 17.

A. DISCUSSION OF THE RESULTS

The measurements in Fig. 14(a)-(c) and Fig. 16(a)-(c) are in agreement with the simulations in Fig. 7 and Fig. 8, respectively. It is possible to notice in Fig. 14(c) and Fig. 16(c) that the ZVS turn-on is achieved at the steady-state operation for both coupling factors. The measured propagation delay introduced by the control circuit has been measured at different load and coupling conditions in Fig. 14(d), Fig. 15(b), and Fig. 16(d). These measurements confirm that

the propagation delay can be considered to be constant. However, to compensate for this delay in different operating conditions, variable V_{ref+} and V_{ref-} are needed to detect the optimized ZVS point $|I_{OFF}| = 2$ A. Additionally, the measured delay has been found to be about 5% lower than the theoretical delay calculated in Table III. This difference in the time delay together with the 1% variation of the measured operating frequency with respect to the simulated one in Section IV translates into slightly different values of V_{ref+} and V_{ref-} with respect to ones resulting from the simulations.

For the same output power of 200 W, the applied V_s is around 10% more than the one in Table II used in the simulations due to the higher losses in the experimental set-up, of which the main contributions are the core losses of the main coils that are not considered in the circuit simulations. This explains the drop in the measured efficiency compared to the theoretical one in Fig. 6.

During the start-up of both Fig. 14(b) and Fig. 16(b), the soft switching is partially lost. This could be mitigated by increasing the value of V_{IOFF}, which is the fixed term of V_{ref} in (8). However, this higher reference would eventually impede the power transfer's start-up, as shown in Fig. 11(b) for the fixed frequency case. Knowing that the anti-parallel diode of low voltage MOSFETs can withstand well reverse recovery, for the sake of simplicity, it becomes acceptable to lose the ZVS turn-on for a few switching cycles.

From the measurements in Fig. 14 and Fig. 16, the effectiveness of the auto-resonant detection method has been demonstrated at different coils' magnetic coupling. However, as explained in Section III-A, the proposed scheme can compensate accurately for the propagation delay also in presence of load variations. This is shown in the measurements of Fig. 15 performed by raising V_{batt} from 40 V to 50 V with respect to Fig. 14. This measurement is relevant because, in the application of e-bikes charging, the load is typically a Lithium-ion battery which voltage V_{batt} rises during the charging process. Since the S-S compensation has a current-source behavior, for the same input voltage and magnetic coupling, the battery current I_{batt} remains unvaried as V_{batt} increases. On the other hand, according to the Kirchhoff voltage law in [49] applied on the equivalent circuit of Fig. 1, the H-bridge inverter current I_{AB} can be expressed as

$$\hat{I}_{AB} = -j\frac{\pi}{2}I_{batt}\frac{R_2 + \dfrac{V_{batt} + I_{batt}R_s}{I_{batt}}}{\omega_0 M} \quad (10)$$

According to (10), the amplitude of I_{AB} increases at higher values of V_{batt} while the system's resonant frequency is not affected. As illustrated in Fig. 2(b), an higher amplitude of I_{AB} requires an increase in the detection references V_{ref+} and V_{ref-} to compensate for the same propagation delay. This discussion is supported by the measurement in Fig. 15 performed at $V_{batt} = 50$ V in which I_{AB}, V_{ref+} and V_{ref-} are higher than in Fig. 14 where $V_{batt} = 40$ V for the same optimized ZVS point $|I_{OFF}| = 2$ A.
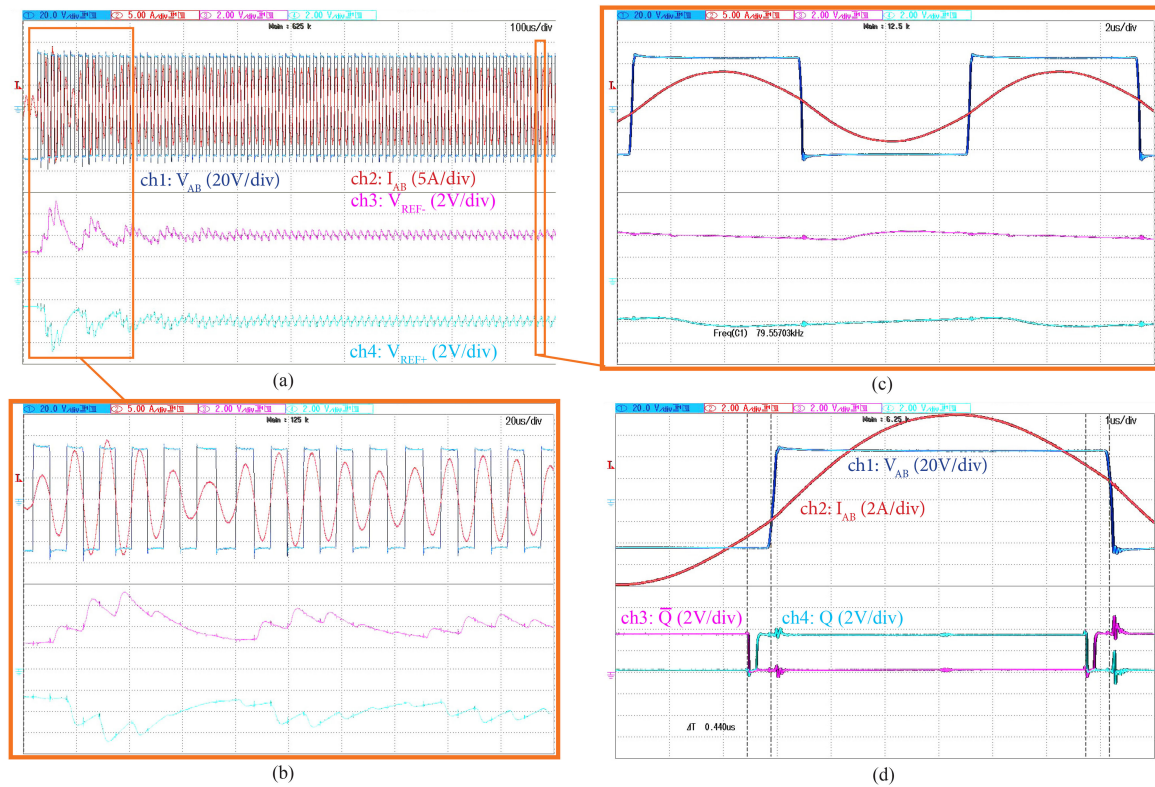
FIGURE 14. Measurements performed with the auto-resonant detection method at k=0.266 and P_{out} = 200 W (V_s = 48 V, V_{batt} = 40 V). Measured V_{AB}, I_{AB}, V_{ref+}, V_{ref-} during: (a) the entire start-up transient; (b) zoom-in on the first start-up cycles; (c) zoom-in on the steady-state operation. (d) Measured propagation delay between the gating control signals Q, $\overline{Q}$ and the occurrence of the optimized ZVS point I_{OFF} = 2 A.
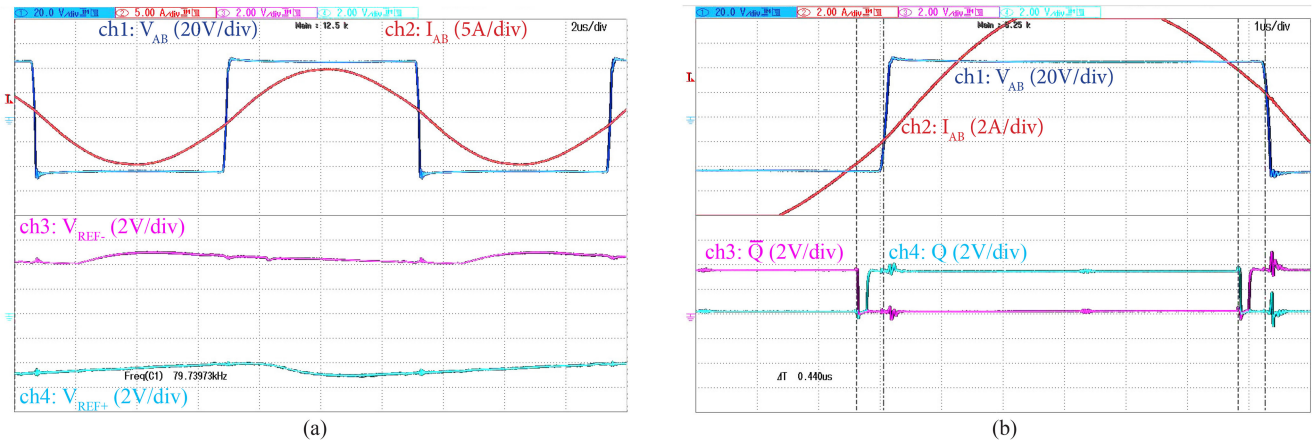

FIGURE 15. Measurements performed with the auto-resonant detection method at k=0.266 and V_{batt} = 50 V (V_s = 48 V, P_{out} > 200 W). This measurement shows the circuit waveforms in the presence of an increase in the load voltage with respect to Fig. 14. (a) Measured V_{AB}, I_{AB}, V_{ref+}, V_{ref-}. (b) Measured propagation delay between the gating control signals Q, $\overline{Q}$ and the occurrence of the optimized ZVS point I_{OFF} = 2 A.

For what concerns the auto-resonant method benchmark against the feedback resonant detection scheme with fixed references, Fig. 17(a)-(b) show the used reference V_{ref} for the current detection and the efficiency $\eta_{DC-to-DC}$ depending on k. Fig. 17(a) has been achieved with the proposed auto-resonant detection, while Fig. 17(b) has been achieved with the controller that uses fixed references. The proposed auto-resonant detector adapts the reference voltage automatically depending on k, while the conventional method with

fixed reference voltage is tuned to one of the operating points. To perform a complete comparison, the fixed reference is considered to be tuned to each one of the three values of k. The colored area in the V_{ref} plots indicates the operating range of k covered by that controller. The lighter areas denote that the operation at that reference voltage is possible for both start-up and steady-state, while the darker ones indicate that the operation is only possible at steady-state. The auto-resonant scheme is operable in the whole range of k for both
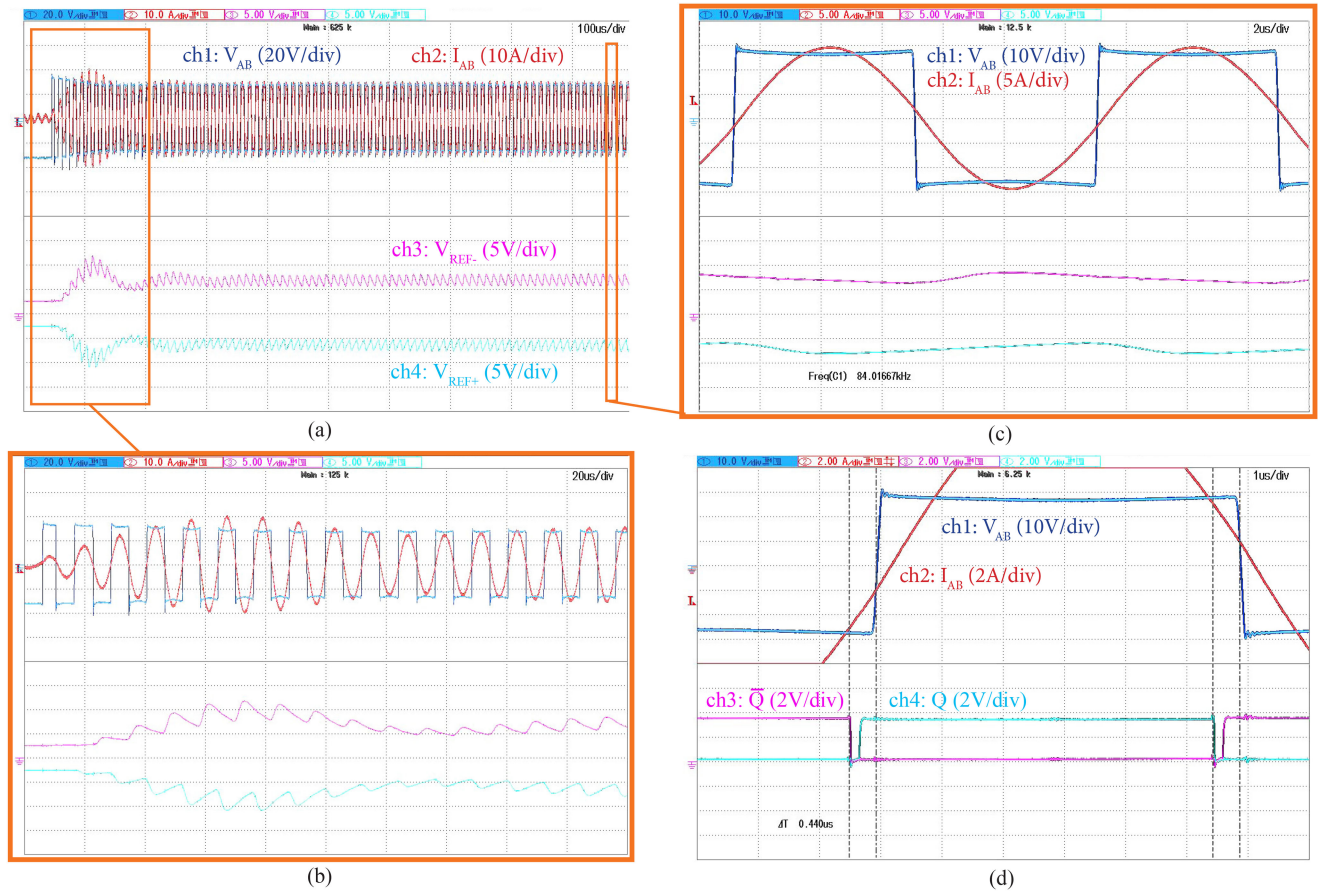
FIGURE 16. Measurements performed with the auto-resonant detection method at k=0.147 and P_{out} = 200 W (V_s = 32.2 V, V_{batt} = 40 V). Measured V_{AB}, I_{AB}, V_{ref+}, V_{ref-} during: (a) the entire start-up transient; (b) zoom-in on the first start-up cycles; (c) zoom-in on the steady-state operation. (d) Measured propagation delay between the gating control signals Q, $\overline{Q}$ and the occurrence of the optimized ZVS point I_{OFF} = 2 A.

the start-up and the steady-state. The conventional method with fixed reference is fully operable only when the reference is tuned at k=0.266, which corresponds to the minimum reference value. On the other hand, the e-bike wireless charging system cannot initiate the power transfer for fixed references tuned at either k=0.201 or k=0.147 because of the higher reference voltage. However, once the charging process is put already in the steady-state condition, the detection would be able to operate with those higher references. Besides the wider operating range, the auto-resonant scheme also translates into higher power transfer efficiency η, up to 1%, given by the ZVS turn-on capability lost in some operating points when using the fixed-reference method. The proof of that is shown in Fig. 17(c)-(e) where the inverter's waveforms at k=0.147 are illustrated, resulting from the fixed references tuned at k=0.266, k=0.201, and from the variable references of the auto-resonant scheme, respectively.

VI. IMPACT OF THE AUTO-RESONANT CONTROL IN HIGHER POWER APPLICATIONS

To reach higher power levels, generally larger DC input voltages are used than the one implemented in the charging of e-bikes. For example, when considering the application of electric cars, the DC input voltage of the 50 kW

IPT system proposed in [52] can be set to a value of 800 V, which is up to 17 times larger than the one used in the proposed 200 W e-bike wireless charging setup. Consequently, the blocking capability of the H-bridge's MOS-FETs (V_{ds}) would also be higher, which might lead to more severe losses in hard-switching conditions. Therefore, it is interesting to preliminary evaluate the benefit of the proposed auto-resonant detection method at higher power levels, particularly its influence on the computed semiconductor switching losses.

For this analysis, the 50 kW IPT system proposed in [52] is considered. This solution represents the state-of-art for future research since 95.8% DC-to-DC peak efficiency has been reached at the rated power level. For what concerns the inverter stage at the primary circuit, a single H-bridge inverter is used, where each switching cell is composed of three paralleled 1200 V SiC MOSFETs, namely C2M0025120D. The parameters used for the switching losses comparison are shown in Table IV which have been extrapolated from the results of [52]. In particular, two magnetic coupling conditions have been considered: $k = k_{max}$ and $k = k_{max}/1.5$. Based on (2), I_{OFF} = 6 A for each SiC MOSFET of the H-bridge inverter ensures the ZVS turn-on in both k conditions. It is reasonable to assume that the resonant frequency f_0 increases
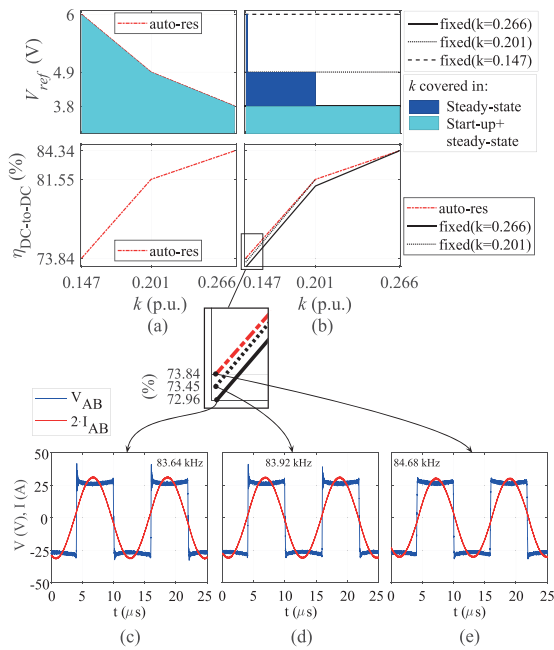
FIGURE 17. Used V_{ref} and measured ηDC-to-DC achieved with: (a) the auto-resonant detection method, (b) the method with fixed references. The lighter coloured areas denote that the operation at that reference voltage is possible for both start-up and steady-state, while the darker ones indicate that the operation is only possible at steady-state. (c)-(e) Measurements at k=0.147, P_{out} = 200 W by using the fixed references tuned at: (c) k=0.266, (d) k=0.201, or with (e) the auto-resonant scheme.

	P_{out} (kW)	η (%)	P_{in} (kW)	I_1 (A)	V_{in} (V)
k_{max} =0.22	50	95.8	52.2	87	672
k_{max}/1.5 =0.147		93.5	53.5	120	495

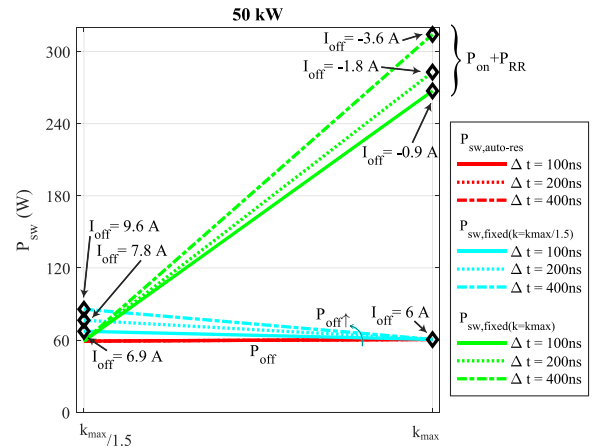|	I_{OFF} (A)	f_0 (kHz)	$V_{ref-}, \|V_{ref+}\|$ (V), for Δt=		
			=100 ns	=200 ns	=400 ns
k_{max} =0.22	6	85	8.2	10.4	14.8
k_{max}/1.5 =0.147		87	9.1	12.2	18.4

FIGURE 18. Comparison of the switching power losses depending on the magnetic coupling k according to the 50 kW IPT system in [52]. Psw,auto-res is the switching loss resulting from the auto-resonant detection method, Psw,fixed(k=k max) and Psw,fixed(k=k max/1.5) are the switching losses resulting from the feedback control with fixed reference tuned at $k = k_{max}$ and $k = k_{max}$/1.5, respectively. The losses are computed for different propagation delay Δt.

by about 2% in the misaligned condition $k = k_{max}/1.5$. This coupling factor corresponds to 120 mm of longitudinal coils' offset with respect to the aligned position, which results into a lower equivalent coils' self-inductance. After that, the detection references V_{ref+} and V_{ref-} can be calculated according to (6)-(8). In this way, the propagation of the delay circuit Δt can be compensated such that the ZVS turn-on in correspondence to I_{OFF} can be achieved. Since this 50 kHz implementation uses an FPGA to process the gating signals, the time delay Δt is unknown and likely to be different than the one measured in Section IV and Section V. For the sake of completeness, three values of Δt have been considered in the calculation of V_{ref+} and V_{ref-}, namely 100 ns, 200 ns, and 400 ns. As expected, the voltage references V_{ref+} and V_{ref-} that detect the same I_{OFF} becomes larger as Δt increases.

The results of the switching losses comparison are shown in Fig. 18 for the three values of Δt and depending on the magnetic coupling condition. In Fig. 18, Psw,auto-res is the switching power loss resulting from the auto-resonant detection method. On the other hand, Psw,fixed(k=k max) and Psw,fixed(k=k max/1.5) are the switching power loss resulting from the feedback control that uses fixed reference voltage tuned at $k = k_{max}$ and $k = k_{max}/1.5$, respectively. The turn-on and turn-off switching energy losses E_{on}, E_{off} of the SiC MOSFET, and reverse recovery charge Q_{RR} of the anti-parallel diode have been extrapolated from the datasheet of C2M0025120D. It is important to point out that the values of

E_{on} and E_{off} depend on the drain current I_D flowing through the MOSFET during the switching instant. Specifically, the switching power losses have been calculated for each MOSFET as

$$P_{on(off)} = E_{on(off)} \cdot f_0 \qquad (11)$$

$$P_{RR} = Q_{RR} \cdot V_{in} \cdot f_0 \qquad (12)$$

From Fig. 18, it is possible to notice that the auto-resonant detection method minimizes the switching losses and keeps them constant over the varying magnetic coupling since it adapts the reference voltage to switch at the same $I_{OFF} = 6$ A. On the other hand, the detection references tuned to the fixed-voltage correspondent to the aligned coupling condition $k = k_{max}$ would result in hard-switching at the lower coupling condition. This occurs because the delay Δt would not be compensated entirely, which results in the H-bridge converter switching at a non-optimal current. This hard-switching operation should be avoided because it increases the switching losses by nearly five times over the auto-resonant detection case, where a considerable contribution comes from the reverse recovery of the anti-parallel diodes. Additionally, the detection references tuned to the more conservative

fixed-voltage correspondent to the lower coupling condition $k = k_{max}/1.5$ would result in higher turn-off losses than in the auto-resonant scheme at the aligned condition. This happens since the detection reference would overcompensate Δt, which translates into a higher I_{OFF}. This scenario is less disadvantageous than the previous one due to the good switching-off behavior of the SiC MOSFETs. However, in reality, this excessively inductive current might affect the total DC-to-DC efficiency of the resonant converter negatively because of the unnecessary circulating reactive power. Additionally, it is clear that both the detection methods with a fixed reference voltage becomes more critical in terms of switching losses in some operating conditions, especially as the propagation delay Δt increases. Additionally, as discussed in Section V-A, the auto-resonant detection method benefits also the tracking of the optimized ZVS point in the presence of load variations.

As a result, the auto-resonant detection method is applicable and beneficial while tracking the resonant frequency also in high power IPT applications.

VII. CONCLUSION

This paper explains and verifies the proposed auto-resonant detection method for the H-bridge converter used in wireless charging applications. The auto-resonant scheme provides a sensible way to track the system's natural resonant frequency by measuring the resonant tank's current. This method's main advantage is that it can achieve the same optimum zero voltage switching turn-on operation at a wide range of magnetic coupling and loading conditions by dynamically compensating for the delay introduced by the control circuit. This is particularly important in wireless charging applications since the operating conditions are generally not fixed, and this variability can be taken to an extreme condition, such as it would be found in dynamic wireless charging. The implementation of the auto-resonant scheme is performed using variable reference levels for the current detection that depends on the current slope at the resonant current's zero-crossing. This concept has been proven mathematically, through simulations, and then experimentally with a 200 W e-bike wireless charging system. The auto-resonant scheme has been benchmarked against the conventional natural resonant frequency detector that uses fixed references. As a result, the auto-resonant scheme extends the operable magnetic coupling and loading range, widens the soft switching region, and improves the DC-to-DC efficiency of the tested e-bike charger of nearly 1%. Furthermore, the proposed auto-resonant scheme has shown considerable benefits also in the high power wireless charging application of 50 kW since it can keep the switching losses of the H-bridge's semiconductors constant over the usable coils' magnetic coupling range.

REFERENCES

[1] K. Agarwal, R. Jegadeesan, Y. Guo, and N. V. Thakor, "Wireless power transfer strategies for implantable bioelectronics," *IEEE Rev. Biomed. Eng.*, vol. 10, pp. 136–161, 2017.

[2] J. Moon, H. Hwang, B. Jo, H. Shin, and S. Kim, "Design of a 5-W power receiver for 6.78 MHz resonant wireless power transfer system with power supply switching circuit," *IEEE Trans. Consum. Electron.*, vol. 62, no. 4, pp. 349–354, Nov. 2016.

[3] M. Lu, M. Bagheri, A. P. James, and T. Phung, "Wireless charging techniques for uavs: A review, reconceptualization, and extension," *IEEE Access*, vol. 6, pp. 29865–29884, 2018.

[4] S. Li and C. C. Mi, "Wireless power transfer for electric vehicle applications," *IEEE Trans. Emerg. Sel. Top. Power Electron.*, vol. 3, no. 1, pp. 4–17, Mar. 2015.

[5] D. Patil, M. K. McDonough, J. M. Miller, B. Fahimi, and P. T. Balsara, "Wireless power transfer for vehicular applications: Overview and challenges," *IEEE Trans. Transp. Electrific.*, vol. 4, no. 1, pp. 3–37, Mar. 2018.

[6] V. Cirimele, M. Diana, F. Freschi, and M. Mitolo, "Inductive power transfer for automotive applications: State-of-the-art and future trends," *IEEE Trans. Ind. Appl.*, vol. 54, no. 5, pp. 4069–4079, Sept./Oct. 2018.

[7] G. Guidi, J. A. Suul, F. Jenset, and I. Sorfonn, "Wireless charging for ships: High-power inductive charging for battery electric and plug-in hybrid vessels," *IEEE Electrific. Mag.*, vol. 5, no. 3, pp. 22–32, Sep. 2017.

[8] C. R. Teeneti, T. T. Truscott, D. N. Beal, and Z. Pantic, "Review of wireless charging systems for autonomous underwater vehicles," *IEEE J. Ocean. Eng.*, vol. 46, no. 1, pp. 68–87, Jan. 2021.

[9] V. Shevchenko, O. Husev, R. Strzelecki, B. Pakhaliuk, N. Poliakov, and N. Strzelecka, "Compensation topologies in IPT systems: Standards, requirements, classification, analysis, comparison and application," *IEEE Access*, vol. 7, pp. 120559–120580, 2019.

[10] J. Garnica, R. A. Chinga, and J. Lin, "Wireless power transmission: From far field to near field," *Proc. IEEE*, vol. 101, no. 6, pp. 1321–1331, Jun. 2013.

[11] B. Clerckx, R. Zhang, R. Schober, D. W. K. Ng, D. I. Kim, and H. V. Poor, "Fundamentals of wireless information and power transfer: From RF energy harvester models to signal and system designs," *IEEE J. Sel. Areas Commun.*, vol. 37, no. 1, pp. 4–33, Jan. 2019.

[12] T. C. Beh, M. Kato, T. Imura, S. Oh, and Y. Hori, "Automated impedance matching system for robust wireless power transfer via magnetic resonance coupling," *IEEE Trans. Ind. Electron.*, vol. 60, no. 9, pp. 3689–3698, Sep. 2013.

[13] Y. Lim, H. Tang, S. Lim, and J. Park, "An adaptive impedance-matching network based on a novel capacitor matrix for wireless power transfer," *IEEE Trans. Power Electron.*, vol. 29, no. 8, pp. 4403–4413, Aug. 2014.

[14] N. Y. Kim, K. Y. Kim, J. Choi, and C. . Kim, "Adaptive frequency with power-level tracking system for efficient magnetic resonance wireless power transfer," *Electron. Lett.*, vol. 48, no. 8, pp. 452–454, 2012.

[15] A. J. Moradewicz and M. P. Kazmierkowski, "Contactless energy transfer system with FPGA-controlled resonant converter," *IEEE Trans. Ind. Electron.*, vol. 57, no. 9, pp. 3181–3190, Sep. 2010.

[16] D. Xu, D. Wang, and J. Li, "Transmitter current tracking method of improving power-transfer efficiency for two-coil wireless power transfer system," in *Proc. Chin. Automat. Congr.*, 2018, 2477–2481.

[17] W. Fu, B. Zhang, and D. Qiu, "Study on frequency-tracking wireless power transfer system by resonant coupling," in *Proc. IEEE 6th Int. Power Electron. Motion Control Conf.*, 2009, pp. 2658–2663.

[18] J. Wang, Z. Zhu, C. Li, J. Huangfu, and L. Ran, "PLL-based self-adaptive resonance tuning for a wireless-powered potentiometer," *IEEE Trans. Circuits Syst. II: Exp. Briefs*, vol. 60, no. 7, pp. 392–396, Jul. 2013.

[19] K. Xie, A. Huang, X. Li, S. Guo, and H. Zhang, "Modular high-voltage bias generator powered by dual-looped self-adaptive wireless power transmission," *Rev. Sci. Instruments*, vol. 86, 2015, Art. no. 044707.

[20] Q. Li and Y. C. Liang, "An inductive power transfer system with a high-q resonant tank for mobile device charging," *IEEE Trans. Power Electron.*, vol. 30, no. 11, pp. 6203–6212, Nov. 2015.

[21] S. Liu, Y. Shen, Y. Wu, J. Lin, and M. Hu, "Study on frequency tracking for wireless power transfer system using magnetic resonant coupling," in *Proc. 13th IEEE Conf. Ind. Electron. Appl.*, 2018, pp. 2569–2572.

[22] Z. Huang, S. Wong, and C. K. Tse, "Comparison of basic inductive power transfer systems with linear control achieving optimized efficiency," *IEEE Trans. Power Electron.*, vol. 35, no. 3, pp. 3276–3286, Mar. 2020.

[23] H. L. Li, A. P. Hu, and G. A. Covic, "Fpga controlled high frequency resonant converter for contactless power transfer," in *Proc. IEEE Power Electron. Specialists Conf.*, 2008, pp. 3642–3647.

[24] H. L. Li, A. P. Hu, G. A. Covic, and C. Tang, "A new primary power regulation method for contactless power transfer," in *Proc. IEEE Int. Conf. Ind. Technol.*, 2009, pp. 1–5.

[25] X. Ren, Q. Chen, L. Cao, X. Ruan, S.-C. Wong, and C. K. Tse, "Characterization and control of self-oscillating contactless resonant converter with fixed voltage gain," in *Proc. 7th Int. Power Electron. Motion Control Conf.*, vol. 3, 2012, pp. 1822–1827.

[26] K. Yan, Q. Chen, J. Hou, X. Ren, and X. Ruan, "Self-oscillating contactless resonant converter with phase detection contactless current transformer," *IEEE Trans. Power Electron.*, vol. 29, no. 8, pp. 4438–4449, Aug. 2014.

[27] L. Xu, Q. Chen, X. Ren, S. Wong, and C. K. Tse, "Self-oscillating resonant converter with contactless power transfer and integrated current sensing transformer," *IEEE Trans. Power Electron.*, vol. 32, no. 6, pp. 4839–4851, Jun. 2017.

[28] K. Xie, A. Huang, L. Chen, S. Guo, and H. Zhang, "Half-cycle resonance tracking for inductively coupled wireless power transmission system," *IEEE Trans. Power Electron.*, vol. 33, no. 3, pp. 2668–2679, Mar. 2018.

[29] H. Zhu, B. Zhang, and L. Wu, "Output power stabilization for wireless power transfer system employing primary-side-only control," *IEEE Access*, vol. 8, pp. 63735–63747, 2020.

[30] Y. Liu, U. K. Madawala, R. Mai, and Z. He, "Zero-phase-angle controlled bidirectional wireless EV charging systems for large coil misalignments," *IEEE Trans. Power Electron.*, vol. 35, no. 5, pp. 5343–5353, May 2020.

[31] J. Zhang, J. Zhao, Y. Zhang, and F. Deng, "A wireless power transfer system with dual switch-controlled capacitors for efficiency optimization," *IEEE Trans. Power Electron.*, vol. 35, no. 6, pp. 6091–6101, Jun. 2020.

[32] R. Bonache-Samaniego, C. Olalla, L. Martínez-Salamero, and D. Maksimovic, "6.78 MHz self-oscillating parallel resonant converter based on gan technology," in *Proc. IEEE Appl. Power Electron. Conf. Expo.*, 2017, pp. 1594–1599.

[33] K. Sabi and D. Costinett, "Noise mitigation and delay compensation in high frequency dual current programmed mode control," in *Proc. IEEE Appl. Power Electron. Conf. Expo.*, 2018, pp. 3095–3101.

[34] K. Sabi and D. Costinett, "Delay mitigation in high frequency dual current programmed mode control gan-based zvs inverter," in *Proc. 20th Workshop Control Model. Power Electron.*, 2019, pp. 1–7.

[35] J. Sun, N. N. Strain, D. J. Costinett, and L. M. Tolbert, "Analysis of a gan-based crm totem-pole PFC converter considering current sensing delay," in *Proc. IEEE Energy Convers. Congr. Expo.*, 2019, pp. 4421–4428.

[36] R. Bosshard, J. W. Kolar, and B. Wunsch, "Control method for inductive power transfer with high partial-load efficiency and resonance tracking," in *Proc. Int. Power Electron. Conf. (IPEC-Hiroshima 2014 - ECCE ASIA)*, 2014, pp. 2167–2174.

[37] H. Li, J. Li, K. Wang, W. Chen, and X. Yang, "A maximum efficiency point tracking control scheme for wireless power transfer systems using magnetic resonant coupling," *IEEE Trans. Power Electron.*, vol. 30, no. 7, pp. 3998–4008, Jul. 2015.

[38] T. Diekhans and R. W. De Doncker, "A dual-side controlled inductive power transfer system optimized for large coupling factor variations and partial load," *IEEE Trans. Power Electron.*, vol. 30, no. 11, pp. 6320–6328, Nov. 2015.

[39] R. Laouamer, M. Brunello, J. P. Ferrieux, O. Normand, and N. Buchheit, "A multi-resonant converter for non-contact charging with electromagnetic coupling," in *Proc. IECON'97 23 rd Int. Conf. Ind. Electron., Control, Instrum.*, vol. 21997, pp. 792–797.

[40] J. T. Boys, G. A. Covic, and A. W. Green, "Stability and control of inductively coupled power transfer systems," *IEE Proc. - Electric Power Appl.*, vol. 147, no. 1, pp. 37–43, 2000.

[41] O. H. Stielau and G. A. Covic, "Design of loosely coupled inductive power transfer systems," in *Proc. PowerCon Int. Conf. Power Syst. Technol. Proc.*, vol. 1 2000, pp. 85–90.

[42] C.-S. Wang, G. A. Covic, and O. H. Stielau, "Power transfer capability and bifurcation phenomena of loosely coupled inductive power transfer systems," *IEEE Trans. Ind. Electron.*, vol. 51, no. 1, pp. 148–157, Feb. 2004.

[43] C.-S. Wang, O. H. Stielau, and G. A. Covic, "Design considerations for a contactless electric vehicle battery charger," *IEEE Trans. Ind. Electron.*, vol. 52, no. 5, pp. 1308–1314, Oct. 2005.

[44] S. Chopra and P. Bauer, "Analysis and design considerations for a contactless power transfer system," in *Proc. IEEE 33 rd Int. Telecommun. Energy Conf.*, 2011, pp. 1–6.

[45] M. Iordache, L. Mandache, D. Niculae, and L. Iordache, "On exact circuit analysis of frequency splitting and bifurcation phenomena in wireless power transfer systems," in *Proc. Int. Symp. Signals, Circuits Syst.*, 2015, pp. 1–4.

[46] R. L. Steigerwald, "A comparison of half-bridge resonant converter topologies," *IEEE Trans. Power Electron.*, vol. 3, no. 2, pp. 174–182, Apr. 1988.

[47] S. Li, W. Li, J. Deng, T. D. Nguyen, and C. C. Mi, "A double-sided LCC compensation network and its tuning method for wireless power transfer," *IEEE Trans. Veh. Technol.*, vol. 64, no. 6, pp. 2261–2273, Jun. 2015.

[48] T. Kan, T. Nguyen, J. C. White, R. K. Malhan, and C. C. Mi, "A new integration method for an electric vehicle wireless charging system using lcc compensation topology: Analysis and design," *IEEE Trans. Power Electron.*, vol. 32, no. 2, pp. 1638–1650, Feb. 2017.

[49] F. Grazian, P. van Duijsen, T. B. Soeiro, and P. Bauer, "Advantages and tuning of zero voltage switching in a wireless power transfer system," in *Proc. IEEE PELS Workshop Emerg. Technol.: Wireless Power Transfer (WoW)*, 2019, pp. 367–372.

[50] F. Grazian, P. van Duijsen, B. Roodenburg, T. B. Soeiro, and P. Bauer, "Auto-resonant control of the h-bridge resonantconverter for inductive power transfer applications," in *Proc. IEEE 29th Int. Symp. Ind. Electron.*, 2020.

[51] G. R. C. Mouli, P. V. Duijsen, F. Grazian, A. Jamodkar, P. Bauer, and O. Isabella, "Sustainable e-bike charging station that enables AC, DC and wireless charging from solar energy," *Energies*, vol. 13, no. 14, pp. 1–21, 2020.

[52] R. Bosshard and J. W. Kolar, "Multi-objective optimization of 50 kW/85 kHz ipt system for public transport," *IEEE Trans. Emerg. Sel. Top. Power Electron.*, vol. 4, no. 4, pp. 1370–1382, Dec. 2016.

FRANCESCA GRAZIAN (Student Member, IEEE) received the bachelor's degree in electrical engineering from the University of Bologna, Bologna, Italy, in 2016 and the master's degree in 2018 in electrical engineering from the Delft University of Technology, Delft, The Netherlands, in 2018, focusing on power electronics. She is currently working toward the Ph.D. degree with the Delft University of Technology.

Her research focuses on developing wireless power transfer.

THIAGO BATISTA SOEIRO (Senior Member, IEEE) received the B.Sc. (Hons.) and M.Sc. degrees in electrical engineering from the Federal University of Santa Catarina, Florianopolis, Brazil, in 2004 and 2007, respectively, and the Ph.D. degree from the Swiss Federal Institute of Technology, Zurich, Switzerland, in 2012.

During the master's and Ph.D. studies, he was a Visiting Scholar with Power Electronics and Energy Research Group, Concordia University, Montreal, QC, Canada, and with the Center for Power Electronics Systems, Blacksburg, VA, USA. From 2012 to 2013, he was a Researcher with the Power Electronics Institute, Federal University of Santa Catarina. From October 2013 to April 2018, he was a Senior Scientist with the Corporate Research Center, ABB Switzerland Ltd., Baden-Dattwil, Switzerland. Since May 2018, he has been with DC Systems, Energy Conversion and Storage Group, Delft University of Technology, Delft, The Netherlands. He is currently an Associate Professor. His research interests include advanced high power converters and dc system integration.

Dr. Soeiro was the recipient of the 2013 IEEE Industrial Electronics Society Best Conference Paper Award and the Best Paper Awards in the following IEEE conferences, International Conference on Power Electronics (ECCE Asia 2011), International Conference on Industrial Technology (ICIT 2013), and Conference on Power Electronics and Applications EPE'15 (ECCE Europe 2015).

PETER VAN DUIJSEN received the master's degree in electrical engineering and the Ph.D. degree in modeling and simulation of power electronic systems in 2013. He has worked on computer simulation and power electronics for nearly 30 years. After receiving the master's degree, and working with the Technical University of Delft, he founded Simulation Research and developed the simulation program CASPOC. He currently heads the Research and Development Department on simulation research. Since 2008, he has been a Guest Lecturer with the Korean University of Technology, Cheonan, South Korea and The Hague University of Applied Science, Hague, The Netherlands, regarding dc grids and storage.

He has coauthored several textbooks in the field of power electronics, drives, solar, wind and e-Vehicles and is involved in the development of educational training hardware in the field of renewable energy.

PAVOL BAUER (Senior Member, IEEE) received master's degree in electrical engineering from the Technical University of Kosice, Kosice, Slovakia, in 1985 and the Ph.D. degree from the Delft University of Technology, Delft, The Netherlands, in 1995.

He is currently a Full Professor with the Department of Electrical Sustainable Energy, Delft University of Technology, and the Head of DC Systems, Energy Conversion and Storage Group. He is the author or coauthor of eight books, holds four international patents, and organized several tutorials at the international conferences. He has worked on many projects for industry concerning wind and wave energy, power electronic applications for power systems, including Smarttrafo, HVDC systems, projects for smart cities such as photovoltaic (PV) charging of electricv ehicles, PV and storage integration, contactless charging, and he participated in several Leonardo da Vinci and H2020 EU projects as a Project Partner, ELINA, INETELE, and E-Pragmatic and a Coordinator, PEMCWebLab.com-Edipe, SustEner, and Eranet DCMICRO.

Prof. Bauer is the Former Chairman of Benelux IEEE Joint Industry Applications Society, Power Electronics and Power Engineering Society Chapter, the Chairman of the Power Electronics and Motion Control Council, a Member of the Executive Committee of European Power Electronics Association, and also a Member of the International Steering Committee at numerous conferences.